

# Quadrangle-grid velocity–stress finite-difference method for elastic-wave-propagation simulation

Zhang Jianfeng

Department of Engineering Mechanics, Dalian University of Technology, Dalian 116023, China. E-mail: zjfhm@gingko.dlut.edu.cn

Accepted 1997 May 28. Received 1997 May 6; in original form 1996 August 28

## SUMMARY

I present a 2-D numerical-modelling algorithm based on a first-order velocity–stress hyperbolic system and a non-rectangular-grid finite-difference operator. In this method the velocity and stress are defined at different nodes for a staggered grid. The scheme uses non-orthogonal grids, thereby surface topography and curved interfaces can be easily modelled in the seismic-wave-propagation stimulation. The free-surface conditions of complex geometry are achieved by using integral equilibrium equations on the surface, and the stability of the free-surface conditions is improved by introducing local filter modification. The method incorporates desirable qualities of the finite-element method and the staggered-grid finite-difference scheme, which is of high accuracy and low computational cost.

**Key words:** elastic-wave theory, seismic modelling, topography.

## INTRODUCTION

Many finite-difference schemes (Virieux 1986; Levander 1988; Kosloff *et al.* 1990; Magnier, Mora & Tarantola 1994) have been developed from the first-order coupled elastic equations of motion and constitutive laws expressed in velocities and stresses. Many of these are stable (for all values of Poisson's ratio) and accurate, making them ideal for modelling marine exploration problems. This feature is usually lacking from finite-difference schemes developed from the second-order coupled elastic equations expressed in displacements (e.g. Kelly *et al.* 1976). The staggered-grid (Virieux 1986; Levander 1988) and minimal-grid (Magnier *et al.* 1994) schemes are of less computational cost; however, they are incapable of handling the complex geometrical surface. The pseudo-spectral method has been adopted to account for surface topography by mapping a rectangular grid onto a curved grid (Tessmer, Kosloff & Behle 1992; Tessmer & Kosloff 1994). However, the implementation of the above map is difficult when incorporating simultaneously the surface topography and other complex geometrical boundaries as well as curved interfaces. The finite-difference technique has been adopted to deal with *SH* motion in complex geometries by using irregular grids (Moczo 1989). The finite-element method (Zienkiewicz 1977) is more flexible in handling complex geometrical boundaries. Unfortunately, this method is more time consuming and requires more computer memory. It is very important to develop a new finite-difference scheme which can serve as a powerful tool for the study of elastic-wave-propagation phenomena in the vicinity of non-planar surfaces and interfaces.

In this paper, I adopt the velocity–stress finite-difference scheme to handle complex geometrical boundaries and interfaces

by introducing a quadrangle-grid finite-difference approximation to derivatives of first-order velocity–stress hyperbolic systems. The free-surface boundary conditions of complex geometries are obtained by applying Gaussian quadrature formula approximation to integral equilibrium equations on the surface, and the numerical stability of the boundary conditions is improved by introducing local filter modifications to the numerical results of the boundary points. The resulting finite-difference scheme incorporates desirable qualities of the finite-element method and the staggered-grid finite-difference scheme, which is of high accuracy and low computational cost. The new scheme is tested against an analytical solution for Lamb's problem to demonstrate the accuracy of this new modelling algorithm. I then present an example of surface-wave propagation in an elastic half-space with a cylindrical pit on the surface. The last example deals with a sinusoidal liquid/solid interface for an explosive source in the liquid. The scheme can readily be extended to three dimensions.

## BASIC CONCEPTS

The first-order system of equations for the velocity and stress (Virieux 1986) are

$$\frac{\partial u_t}{\partial t} = \frac{1}{\rho} \left( \frac{\partial \sigma_x}{\partial x} + \frac{\partial \tau_{xz}}{\partial z} \right), \quad (1)$$

$$\frac{\partial w_t}{\partial t} = \frac{1}{\rho} \left( \frac{\partial \tau_{xz}}{\partial x} + \frac{\partial \sigma_z}{\partial z} \right), \quad (2)$$

$$\frac{\partial \sigma_x}{\partial t} = (\lambda + 2\mu) \frac{\partial u_t}{\partial x} + \lambda \frac{\partial w_t}{\partial z}, \quad (3)$$

$$\frac{\partial \sigma_z}{\partial t} = \lambda \frac{\partial u_t}{\partial x} + (\lambda + 2\mu) \frac{\partial w_t}{\partial z}, \quad (4)$$

$$\frac{\partial \tau_{xz}}{\partial t} = \mu \left( \frac{\partial u_t}{\partial z} + \frac{\partial w_t}{\partial x} \right), \quad (5)$$

where  $u_t$  and  $w_t$  are the particle velocity components in  $x$  and  $z$ ,  $\lambda$  and  $\mu$  are the Lamé coefficients, and  $\rho$  is the density. Many finite-difference schemes are based on solving the above equations. The key procedures of these are: (1) calculating time derivatives of the velocity components from eqs (1) and (2) by using finite-difference approximations to first-order space derivatives of the stress at time  $t$  and then obtaining particle velocities at time  $t + \Delta t/2$  using time integration; (2) calculating time derivatives of the stress components from eqs (3)–(5) by using finite-difference approximations to first-order space derivatives of the velocity at time  $t + \Delta t/2$  and then obtaining the stresses at time  $t + \Delta t$  using time integration. Stresses and velocities are thus updated in a staggered time grid. Virieux (1986) and Levander (1988) defined the spatial finite-difference operator in the orthogonal grids and Magnier (1994) defined that in the equilateral-triangle grids, hence all these methods can only solve problems with standard geometrical boundaries. In this paper I enable the velocity–stress finite-difference scheme to handle complex geometrical boundaries by introducing a non-rectangular-grid finite-difference operator.

The non-rectangular-grid finite-difference operator is defined in non-orthogonal grids, which means that the approximation to spatial derivatives can be achieved by using field variable values at four corner nodes of an arbitrary quadrangle. In order to obtain the non-rectangular-grid finite-difference operator, I map the arbitrary quadrangle in the  $(x, z)$ -domain into a square of  $(\xi, \eta)$ -coordinates. The mapping functions are:

$$x = \frac{1}{4}(1 + \xi)(1 + \eta)x_1 + \frac{1}{4}(1 - \xi)(1 + \eta)x_2 + \frac{1}{4}(1 - \xi)(1 - \eta)x_3 + \frac{1}{4}(1 + \xi)(1 - \eta)x_4, \quad (6)$$

$$z = \frac{1}{4}(1 + \xi)(1 + \eta)z_1 + \frac{1}{4}(1 - \xi)(1 + \eta)z_2 + \frac{1}{4}(1 - \xi)(1 - \eta)z_3 + \frac{1}{4}(1 + \xi)(1 - \eta)z_4 \quad (7)$$

where  $(x_i, z_i)$ ,  $i = 1, 2, 3, 4$ , are the coordinates of the quadrangle nodes in the  $(x, z)$ -domain. The derivatives of the field variable  $P(x, z)$  with respect to  $(\xi, \eta)$ -coordinates can be expressed as follows:

$$\begin{aligned} \frac{\partial P}{\partial \xi} &= \frac{\partial P}{\partial x} \frac{\partial x}{\partial \xi} + \frac{\partial P}{\partial z} \frac{\partial z}{\partial \xi}, \\ \frac{\partial P}{\partial \eta} &= \frac{\partial P}{\partial x} \frac{\partial x}{\partial \eta} + \frac{\partial P}{\partial z} \frac{\partial z}{\partial \eta}. \end{aligned} \quad (8)$$

From eq. (8) we obtain

$$\begin{pmatrix} \frac{\partial P}{\partial x} \\ \frac{\partial P}{\partial z} \end{pmatrix} = \begin{bmatrix} \frac{\partial x}{\partial \xi} & \frac{\partial z}{\partial \xi} \\ \frac{\partial x}{\partial \eta} & \frac{\partial z}{\partial \eta} \end{bmatrix}^{-1} \begin{pmatrix} \frac{\partial P}{\partial \xi} \\ \frac{\partial P}{\partial \eta} \end{pmatrix}, \quad (9)$$

where the inverse of the matrix can be solved from eqs (6) and (7) (Zienkiewicz 1977).

With  $P_i$ ,  $i = 1, 4$ , denoting field variable values at the four corner nodes of the quadrangle, the field variable  $P(x, z)$  in the  $(\xi, \eta)$ -domain can be expressed in the form of interpolation as

$$P = \frac{1}{4}(1 + \xi)(1 + \eta)P_1 + \frac{1}{4}(1 - \xi)(1 + \eta)P_2 + \frac{1}{4}(1 - \xi)(1 - \eta)P_3 + \frac{1}{4}(1 + \xi)(1 - \eta)P_4. \quad (10)$$

From eq. (10), we obtain

$$\begin{pmatrix} \frac{\partial P}{\partial \xi} \\ \frac{\partial P}{\partial \eta} \end{pmatrix} = \frac{1}{4} \begin{bmatrix} 1 + \eta & -1 - \eta & -1 + \eta & 1 - \eta \\ 1 + \xi & 1 - \xi & -1 + \xi & -1 - \xi \end{bmatrix} \begin{pmatrix} P_1 \\ P_2 \\ P_3 \\ P_4 \end{pmatrix}. \quad (11)$$

By substituting eq. (11) into eq. (9) we obtain the finite-difference operator for calculating first-order derivatives of the field variables in the inside of the arbitrary quadrangle with the field-variable values at the four nodes. Since the interpolation of eq. (10) makes the field variables conform on boundaries of meshes, the operator presented here is more accurate than the usual formulae obtained through interpolating field variables in the  $(x, z)$ -domain and then calculating the derivatives directly (Zienkiewicz 1977).

The new scheme is illustrated in Fig. 1, where the non-rectangular solid-line grids are generated taking into account boundary and interface geometries, and the dashed-line grids are generated by linking all the centres of the quadrangles. The two velocity components are defined at the nodes of solid-line grids and the three stress components are defined at the nodes of dashed-line grids. Substituting the velocities  $u_t$  and  $w_t$  at four groups of points,  $(a, b, c, m)$ ,  $(m, c, d, e)$ ,  $(m, e, f, g)$  and  $(m, g, h, a)$ , into eqs (11) and (9) gives a finite-difference approximation to the first-order space derivatives of velocities at points  $i, j, k$  and  $l$ ; we can then compute the time derivatives

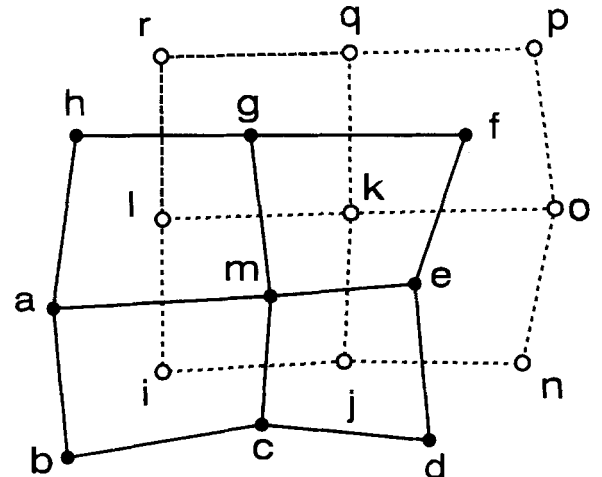


**Figure 1.** Staggered-grid and spatial models for the velocity and stress update. The two velocity components are defined at the nodes of solid-line grids, represented by black dots. The three stress components are defined at the nodes of dashed-line grids, represented by circles.

of stresses  $\sigma_x$ ,  $\sigma_z$  and  $\tau_{xz}$  from eqs (3)–(5) at time-level  $t_0$ , so stresses  $\sigma_x$ ,  $\sigma_z$  and  $\tau_{xz}$  at points  $i$ ,  $j$ ,  $k$  and  $l$  at time-level  $t_0 + \Delta t/2$  are obtained by time integration. Substituting the stress components at points  $i$ ,  $j$ ,  $k$  and  $l$  into eqs (1) and (2) gives the time derivatives of the velocities  $u_i$  and  $w_i$  at point  $m$  by using difference formulae of eqs (9) and (11) at time-level  $t_0 + \Delta t/2$ , thus velocity components at point  $m$  at time-level  $t_0 + \Delta t$  can be obtained by time integration. The velocity components at points  $a$ ,  $b$ ,  $c$ ,  $d$ ,  $e$ ,  $f$ ,  $g$  and  $h$  at time level  $t_0 + \Delta t$  can be solved in the same way. Furthermore, the whole velocity field is updated using this way. The stress field can be updated by analogous spatial stencils from time-level  $t_0 + \Delta t/2$  to time-level  $t_0 + 3\Delta t/2$ .

## BOUNDARY CONDITIONS

Internal interfaces are incorporated naturally by changes of elastic parameters and density in the formulation. The boundary conditions on the edges of the domain of computation, except for the surface, can be treated with the radiation conditions for the modelling of a semi-infinite space. Radiation conditions have been studied by many authors (e.g. Clayton & Engquist 1977), so in this paper only the free-surface boundary conditions in the presence of surface topography are discussed in detail.

The local grids accounting for surface topography are shown in Fig. 2, where points  $a$ ,  $f$  and  $e$  are grid nodes on the surface boundary. With  $h$  and  $j$  denoting the centres of the quadrangles  $abcf$  and  $fcde$ , and  $g$ ,  $i$  and  $k$  denoting the centres of the lines  $af$ ,  $fc$  and  $fe$ , the integral equilibrium equations over the domain enclosed by contour  $ghijkf$  are expressed as follows:

$$\oint_{ghijkf} (\sigma_x l + \tau_{xz} m) ds = \iint \rho \frac{\partial u_i}{\partial t} dx dz, \quad (12)$$

$$\oint_{ghijkf} (\sigma_z m + \tau_{xz} l) ds = \iint \rho \frac{\partial w_i}{\partial t} dx dz,$$

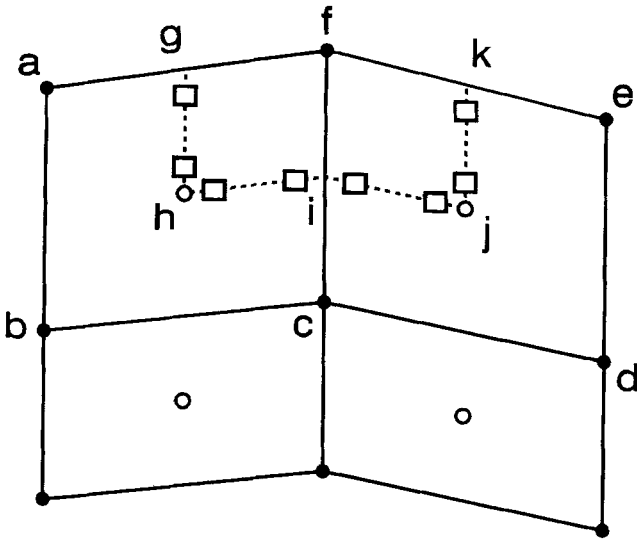


**Figure 2.** Local grids with surface topography. The velocity components are defined at the nodes represented by black dots and stress components are defined at the points represented by circles and squares. The points  $a$ ,  $f$  and  $e$  are on the surface and Gaussian points on line  $gh$ ,  $hi$ ,  $ij$  and  $jk$  are indicated by squares.

where  $l$  and  $m$  are direction cosines of outward-directed normals to the contour  $ghijkf$ . The surface integrals of the right-hand side of the above equations can be approximated by  $M_f(\partial u_i/\partial t)_f$  and  $M_f(\partial w_i/\partial t)_f$ , respectively. Here,  $M_f$  is one-quarter of the sum of the masses of the area enclosed by quadrangle  $abcf$  and that enclosed by quadrangle  $fcde$ , and  $(\partial u_i/\partial t)_f$  and  $(\partial w_i/\partial t)_f$  are, respectively, time derivatives of the velocities  $u_i$  and  $w_i$  at point  $f$ . To cut the contour integral into five parts, an integral over the line  $gfk$  and another four integrals over the lines  $gh$ ,  $hi$ ,  $ij$  and  $jk$ , we know that the first integral is equivalent to the known total load acting on the local boundary  $gfk$ , and the other four integrals can be evaluated by using two-point Gaussian quadrature formula. In the spatial models of Fig. 2, the velocity components are defined at points represented by black dots, and the stress components are defined at points represented by circles and are also defined at eight Gaussian points indicated by squares. The stresses at the Gaussian points can be computed in the same way as calculating the stresses at points  $h$  and  $j$ . Therefore,  $(\partial u_i/\partial t)_f$  and  $(\partial w_i/\partial t)_f$  can be solved from eq. (12), and then the velocity components at point  $f$  on the surface are obtained using time integration. The whole velocity field on the surface can be updated in the manner described above.

It has been observed that instabilities in solving hyperbolic equations are frequently caused by the treatment of the free-surface boundary conditions (Gottlieb, Gunzburger 1982; Kosloff *et al.* 1990). In order to improve the stability of the scheme presented here, we further filter the numerical solutions of the surface nodes achieved above. The local filter modification can be fulfilled by

$$(\tilde{u}_i)_f = \beta(u_i)_f + \frac{1-\beta}{2}[(u_i)_a + (u_i)_e], \quad (13)$$

where  $(u_i)_f$  is the horizontal velocity component at point  $f$  obtained using the free-surface conditions of eq. (12),  $(u_i)_a$  and  $(u_i)_e$  are the horizontal velocity components at points adjacent to point  $f$  (see Fig. 2) obtained using the same free-surface conditions,  $\beta$  is a parameter that is selected in the domain  $0.5 \leq \beta \leq 1.0$  and  $(\tilde{u}_i)_f$  is the modification value of the horizontal velocity component which will replace  $(u_i)_f$  to update the velocity field on the surface. Here,  $\beta = 0.8$ . The vertical velocity component at point  $f$  also needs to be modified in the same way, and these modifications should be carried out for all the nodes on the surface.

## STABILITY ANALYSIS

To analyse stability and dispersion properties, we assume a uniform infinite medium which supports a plane wave. Replacing differential operators with finite-difference operators in eqs (1)–(5) and substituting eqs (3)–(5) into eqs (1) and (2) provides a second-order system of difference equations in velocities only. This system can be written in matrix form using the second-order finite-difference operators  $D_{xx}$ ,  $D_{xz}$ ,  $D_{zz}$  and  $D_{tt}$ :

$$\begin{bmatrix} \alpha^2 D_{xx} + \beta^2 D_{zz} - D_{tt} & (\alpha^2 - \beta^2) D_{xz} \\ (\alpha^2 - \beta^2) D_{xz} & \beta^2 D_{xx} + \alpha^2 D_{zz} - D_{tt} \end{bmatrix} \begin{Bmatrix} u_i \\ w_i \end{Bmatrix} = \begin{Bmatrix} 0 \\ 0 \end{Bmatrix}, \quad (14)$$

where  $\beta = \sqrt{\mu/\rho}$  is the  $S$ -wave velocity and  $\alpha = \sqrt{(\lambda + 2\mu)/\rho}$  is the  $P$ -wave velocity. The finite-difference operator presented

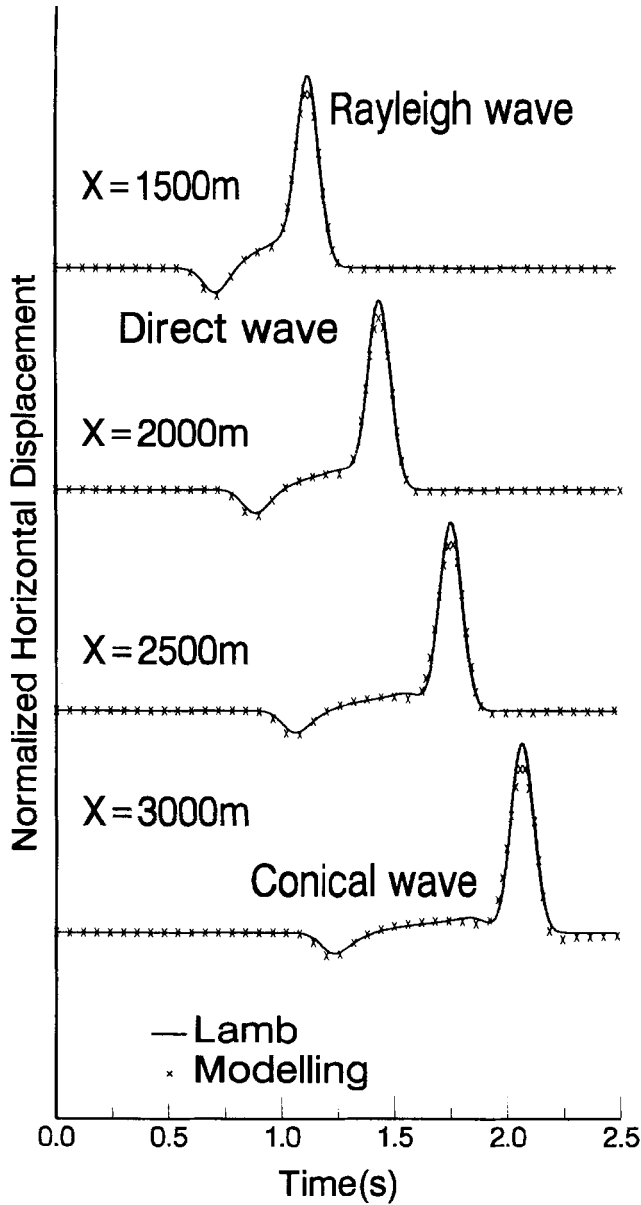


Figure 3. Comparison between numerical and analytical horizontal components for Lamb's problem at different stations on the free surface.

in this paper will vary with changes in the geometry of the quadrangle mesh. For simplicity, we discuss the case when the quadrangle is a parallelogram with an internal angle of  $\theta$ . Let one side of the parallelogram parallel the  $z$ -axis. With  $\Delta x$  and  $\Delta z$  denoting the lengths of two sides of the parallelogram, the second-order finite-difference operators can be expressed as follows:

$$D_{xx}P_{m,n}^j = \frac{1}{4\Delta x^2 \sin^2 \theta} (P_A^j + P_B^j) - \frac{\cos \theta}{2\Delta x \Delta z \sin^2 \theta} P_C^j + \frac{\cos^2 \theta}{4\Delta z^2 \sin^2 \theta} (P_A^j - P_B^j), \quad (15)$$

$$D_{zz}P_{m,n}^j = \frac{1}{4\Delta z^2} (P_A^j - P_B^j), \quad (16)$$

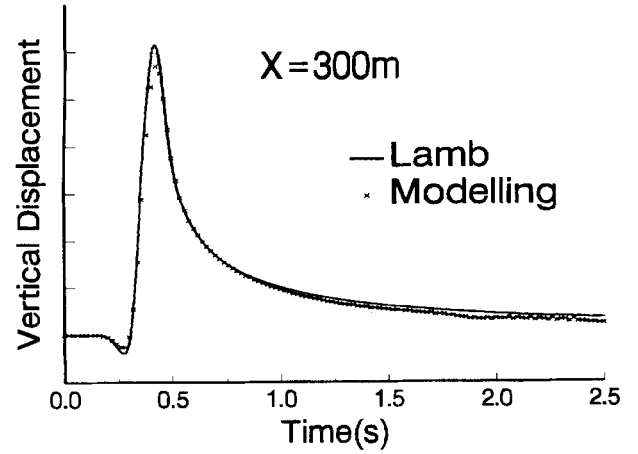


Figure 4. Comparison between numerical and analytical vertical components for Lamb's problem at a source-receiver distance of 300 m on the free surface.

$$D_{xz}P_{m,n}^j = \frac{1}{4\Delta x \Delta z \sin \theta} P_C^j - \frac{\cos \theta}{4\Delta z^2 \sin \theta} (P_A^j - P_B^j), \quad (17)$$

$$D_{tt}P_{m,n}^j = \frac{1}{\Delta t^2} (P_{m,n}^{j+1} + P_{m,n}^{j-1} - 2P_{m,n}^j), \quad (18)$$

where  $j$  is the index for time discretization,  $m$  for grid lines that parallel the  $z$ -axis,  $n$  for another group of grid lines, and

$$P_A^j = P_{m+1,n+1}^j + P_{m-1,n+1}^j + P_{m+1,n-1}^j + P_{m-1,n-1}^j - 4P_{m,n}^j,$$

$$P_B^j = 2P_{m+1,n}^j + 2P_{m-1,n}^j - 2P_{m,n-1}^j - 2P_{m,n+1}^j,$$

$$P_C^j = P_{m+1,n+1}^j + P_{m-1,n-1}^j - P_{m-1,n+1}^j - P_{m+1,n-1}^j.$$

Let the frequency of the plane wave be  $\omega$  and the wave numbers in the  $x$ - and  $z$ -directions be, respectively,  $k_x$  and  $k_z$ . The velocity components at grid point  $(m, n)$  at the time-level  $j$  are

$$\{(u_t)_{m,n}^j, (w_t)_{m,n}^j\}^T = \{u_0, w_0\}^T \exp[i(k_1 m \Delta x + k_2 n \Delta z - \omega j \Delta t)], \quad (19)$$

where  $\{u_0, w_0\}^T$  is the velocity vector at  $(0, 0)$  at the initial time level and  $k_1 = k_x \sin \theta + k_z \cos \theta$ ,  $k_2 = k_z$ . Substituting eq. (19) into eqs (15)–(18) and then substituting the finite-difference operators into eq. (14) gives the following:

$$\begin{bmatrix} \alpha^2 \left( \frac{s_1}{\sin \theta} - \frac{s_2}{\tan \theta} \right)^2 + \beta^2 s_2^2 - s_0 & (\alpha^2 - \beta^2) s_2 \left( \frac{s_1}{\sin \theta} - \frac{s_2}{\tan \theta} \right) \\ (\alpha^2 - \beta^2) s_2 \left( \frac{s_1}{\sin \theta} - \frac{s_2}{\tan \theta} \right) & \beta^2 \left( \frac{s_1}{\sin \theta} - \frac{s_2}{\tan \theta} \right)^2 + \alpha^2 s_2^2 - s_0 \end{bmatrix} \times \begin{Bmatrix} u_0 \\ w_0 \end{Bmatrix} = \begin{Bmatrix} 0 \\ 0 \end{Bmatrix}, \quad (20)$$

where  $s_1 = (2/\Delta x) \sin[(k_1 \Delta x)/2] \cos[(k_2 \Delta z)/2]$ ,  $s_2 = 2/\Delta z \times \sin[(k_2 \Delta z)/2] \cos[(k_1 \Delta x)/2]$ ,  $s_0 = 4/\Delta t^2 \sin^2[(\omega \Delta t)/2]$ . It should be noted that there should be a non-zero solution for the vector  $\{u_0, w_0\}^T$  in eq. (20). Hence, the matrix in eq. (20) must

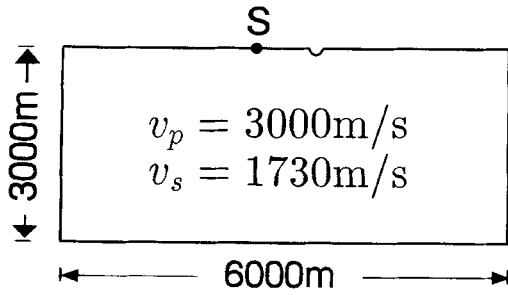


**Figure 5.** Elastic half-space with a cylindrical pit on the surface. The dimensions of the model are 6000 m in the horizontal direction and 3000 m in the vertical direction. The source is located at the surface shown by a black dot. The distance between the source and the pit is 800 m. The cylindrical pit has a radius of 40 m.

be singular, that is we obtain the following:

$$\begin{aligned} & \left[ \alpha^2 \left( \frac{s_1}{\sin \theta} - \frac{s_2}{\tan \theta} \right)^2 + \beta^2 s_2^2 - s_0 \right] \\ & \times \left[ \beta^2 \left( \frac{s_1}{\sin \theta} - \frac{s_2}{\tan \theta} \right)^2 + \alpha^2 s_2^2 - s_0 \right] \\ & - (\alpha^2 - \beta^2)^2 s_2^2 \left( \frac{s_1}{\sin \theta} - \frac{s_2}{\tan \theta} \right)^2 = 0. \end{aligned} \quad (21)$$

Substituting  $s_0$  into eq. (21) we obtain the dispersion relations for the new scheme as follows:

$$\begin{aligned} \sin^2 \left( \frac{\omega \Delta t}{2} \right) &= \frac{\Delta t^2 \alpha^2}{4 \sin^2 \theta} (s_1^2 - 2s_1 s_2 \cos \theta + s_2^2), \\ \sin^2 \left( \frac{\omega \Delta t}{2} \right) &= \frac{\Delta t^2 \beta^2}{4 \sin^2 \theta} (s_1^2 - 2s_1 s_2 \cos \theta + s_2^2). \end{aligned} \quad (22)$$

For stability we require that the frequency  $\omega$  in eq. (19) is a real number, that is  $\sin^2[(\omega \Delta t)/2] \leq 1.0$ . Since  $\alpha^2 \geq \beta^2$ , through substituting  $s_1$  and  $s_2$  into eq. (22) the stability criterion is given by

$$\begin{aligned} & \frac{\Delta t^2 \alpha^2}{\sin^2 \theta} \left[ \frac{1}{\Delta x^2} \sin^2 \left( \frac{k_1 \Delta x}{2} \right) \cos^2 \left( \frac{k_2 \Delta z}{2} \right) \right. \\ & \quad \left. + \frac{1}{\Delta z^2} \sin^2 \left( \frac{k_2 \Delta z}{2} \right) \cos^2 \left( \frac{k_1 \Delta x}{2} \right) \right. \\ & \quad \left. - \frac{\cos \theta}{2 \Delta x \Delta z} \sin(k_1 \Delta x) \sin(k_2 \Delta z) \right] \leq 1.0. \end{aligned} \quad (23)$$

Let  $\Delta x \geq \Delta z$  (or  $\Delta z \geq \Delta x$ ). The stability criterion can be approximately reduced to

$$\Delta t \leq \sin \theta \Delta z / \alpha. \quad (24)$$

From the stability criterion of eq. (24), it is seen that the stability of the scheme presented in this paper is independent of the S-wave velocity and the Poisson's ratio. The algorithm is thus stable for all values of Poisson's ratio and can similarly be used for modelling elastic-wave propagation in materials with a high Poisson's ratio.

It is difficult to analyse the stability of the free-surface conditions analytically, which couples the effects of the discretization of motion equations and the treatment of the free-surface conditions and involves the cumulation of multi-reflections at the surface. The good stability of the free-surface conditions presented in this paper can be demonstrated using numerical examples. Without the filtering of eq. (13), the numerical result would appear to oscillate after many time-step calculations. From a numerical point of view, the filtering of eq. (13) can be considered to be some extent of the average of the wave amplitude in the time domain due to the

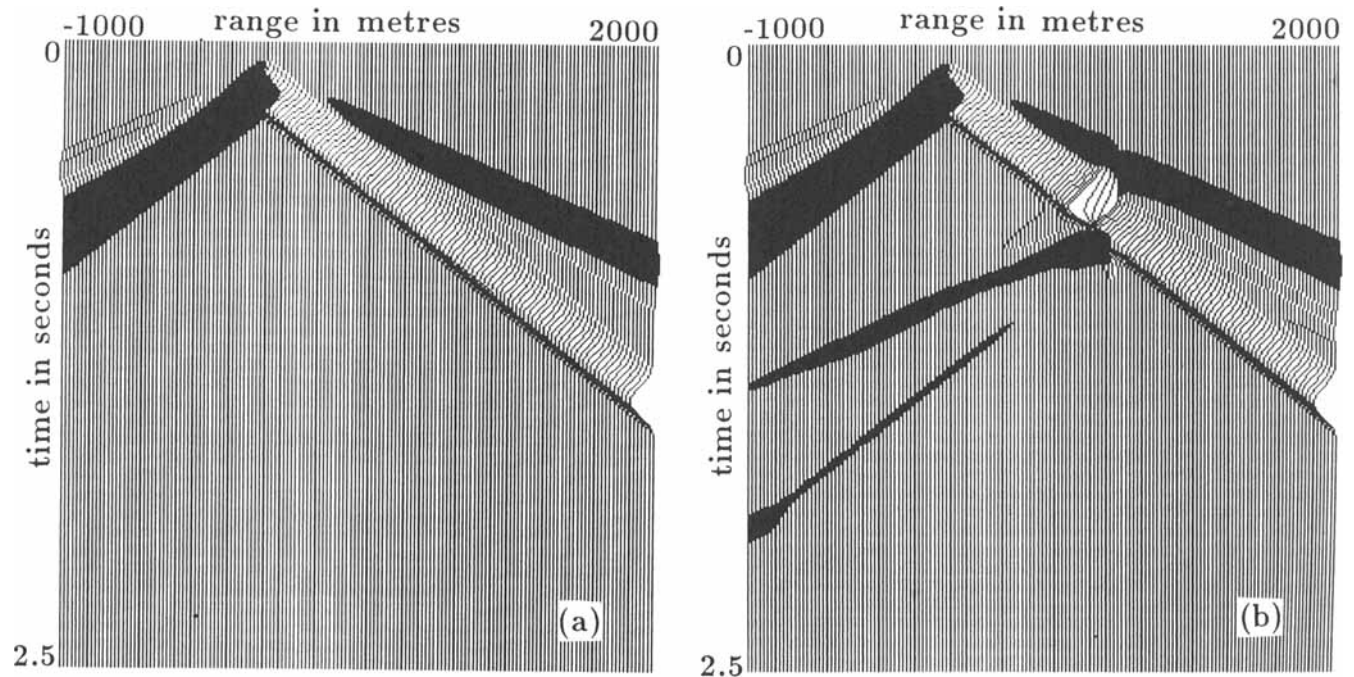


**Figure 6.** Numerical seismograms of the horizontal components of the displacements at the free surface for the half-space with a plane surface (a) and with a pitted surface topography (b).

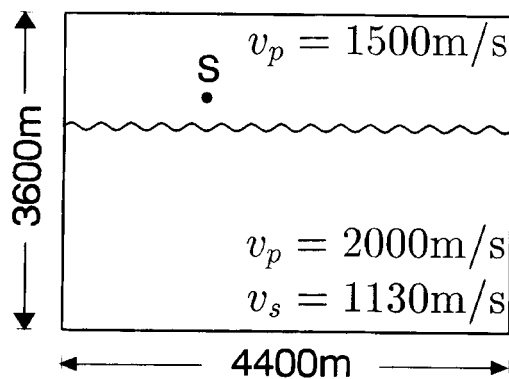


**Figure 7.** Model with a water layer above an elastic half-space with sinusoidal topography of the sea bottom. The interface has a depth of  $1300 \pm 30$  m. The source is located 200 m above the liquid/solid interface.

similarity of wave motions in space and time. The origin of the oscillation is avoided using the filtering of eq. (13).

### ANALYTIC COMPARISON

The accuracy of the numerical modelling algorithm is tested through a comparison of numerical results with an analytical solution of Lamb's problem. Fig. 3 shows the horizontal component due to a vertical Gaussian point source  $f(t) = \exp(-\alpha(t - t_0)^2)$ , with  $\alpha = 200$  and  $t_0 = 0.178$ . Fig. 4 shows the vertical component due to the same source. The surface wave propagates without dispersion and the conical wave builds up. The numerical Rayleigh wave has a slightly lower amplitude than does the analytical Rayleigh wave due to the local filter modification (see eq. 13). Except for this slight misfit, the numerical solutions agree well with the analytical solutions. The total propagation time is 2.5 s with time steps of 4 ms. The semi-infinite medium has a  $P$ -wave velocity of  $3000 \text{ m s}^{-1}$  and an  $S$ -wave velocity of  $1730 \text{ m s}^{-1}$ .

The model is made up of square grids with a grid spacing of 20 m in both the horizontal and the vertical directions. 40 grid points per  $P$  wavelength and 23 grid points per  $S$  wavelength are used in the computation.

### NUMERICAL EXAMPLES

#### Pit on the free surface

In the first example we compare wave propagation in two models which differ in the surface topography. The first model has a plane surface, whereas the second has a cylindrical pit on the surface, as shown in Fig. 5. The cylindrical pit has a radius of 40 m. A vertical Gaussian point-source  $f(t) = \exp(-\alpha(t - t_0)^2)$ , with  $\alpha = 200$  and  $t_0 = 0.178$ , is applied to the surface at the point indicated by a black dot. The distance between the source and the pit is 800 m. The semi-infinite medium has a  $P$ -wave velocity of  $3000 \text{ m s}^{-1}$  and an  $S$ -wave velocity of  $1730 \text{ m s}^{-1}$ . The grid spacing is 20 m in both the horizontal and the vertical directions. The grids of the second model, whose grid spacings in the vicinity of the pit are less than 20 m, are non-orthogonal for modelling the surface topography. 40 grid points per  $P$  wavelength and 23 grid points per  $S$  wavelength are used in the computations.

Fig. 6 shows seismograms of the horizontal component of the displacements. The receivers are located at the surface from  $-1000$  to  $2000$  m (source at zero) with a spacing of 20 m. The seismogram for the half-space with a plane surface is shown on the left-hand side of the figure and the seismogram for the half-space with a cylindrical pit is shown on the right. The difference in the seismograms is remarkable: diffractions due to the pit can be seen clearly.

For a medium of size  $300 \times 150$ , each computation takes about 90 min on a 486 microcomputer to perform 625 time steps of 4 ms. If the finite-element method is used for solving a problem of the same size, a computer memory of more than 100 M is needed. Hence, it is impossible to solve the problem with the finite-element method on a microcomputer.

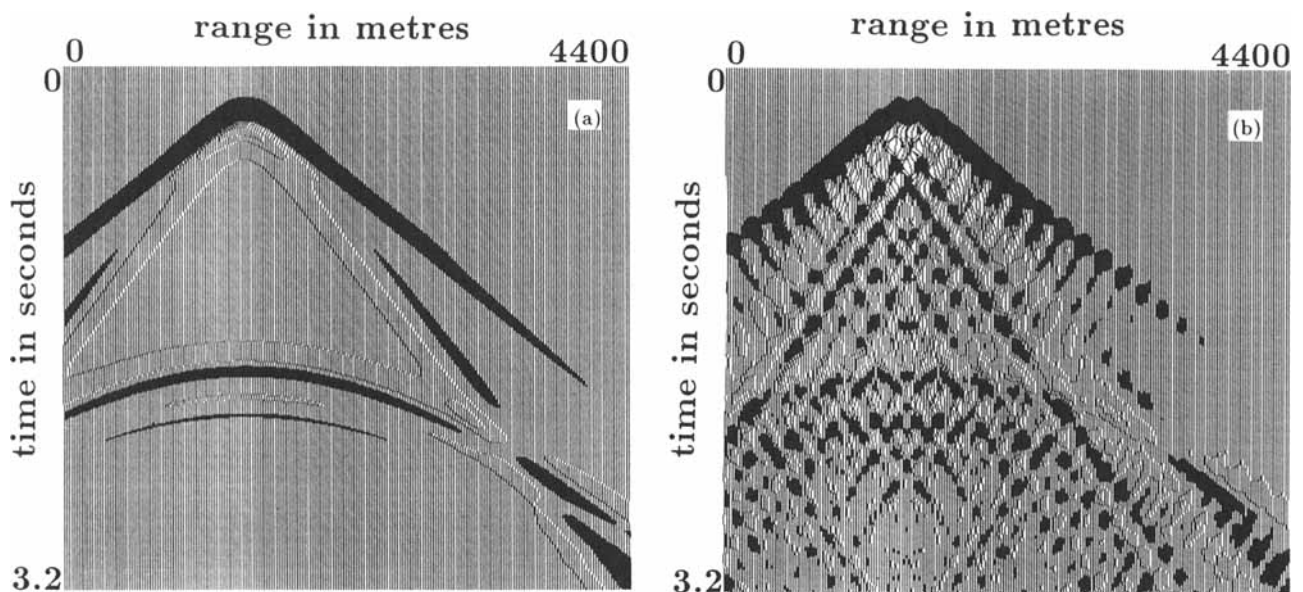


**Figure 8.** Numerical seismograms of the vertical component of the partial velocity for two models with a plane bottom (a) and with a sinusoidal interface (b). The receivers are located at the sea bottom in both cases.

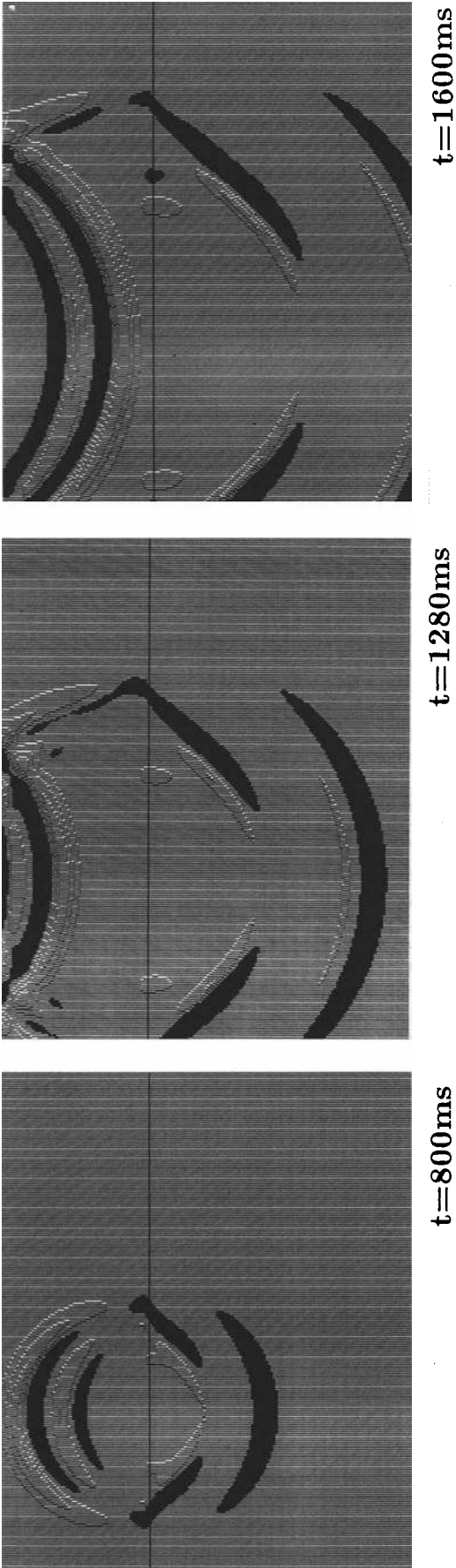


Figure 9. Snapshots of the wavefield for the model with a plane bottom. The displays are for the vertical component of the particle velocity at propagation times of 800, 1280 and 1600 ms.

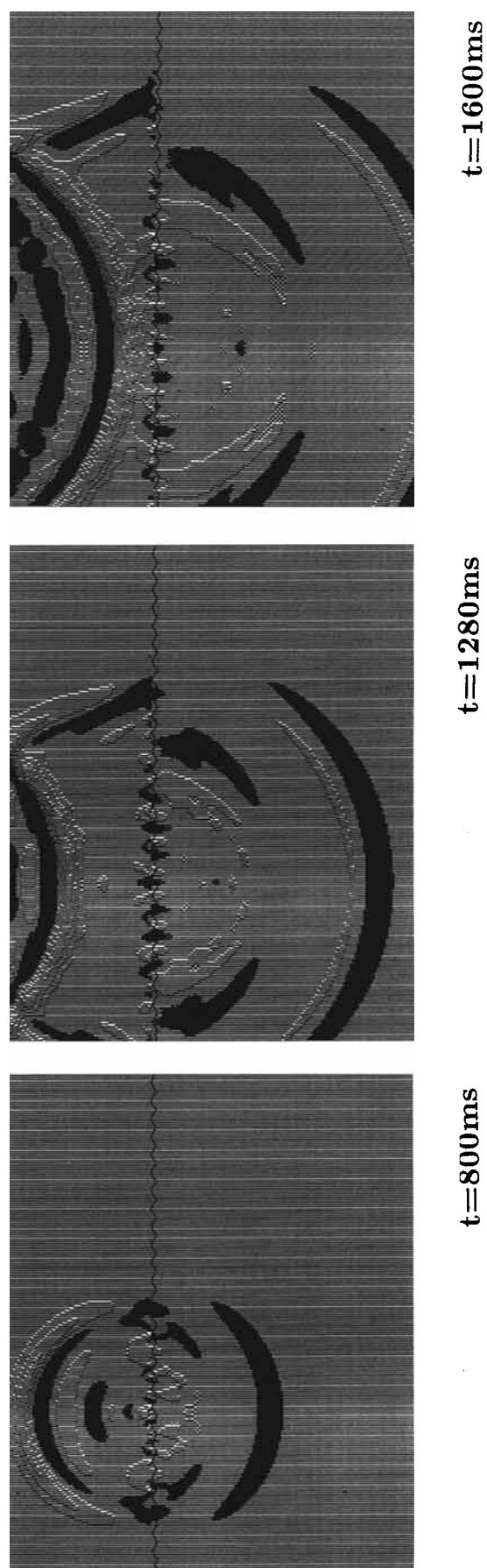


Figure 10. Snapshots of the wavefield for the model with a sinusoidal interface. The displays are for the vertical component of the particle velocities at propagation times of 800, 1280 and 1600 ms.

### Sinusoidal acoustic/elastic interface

In a second example, we present a comparison of two models with a liquid layer on the top of an elastic half-space. In the real world such a model could represent a water layer over rock. The two models only differ in the topography of the ocean bottom. The first model has a plane bottom and the second has a sinusoidal topography, as shown in Fig. 7. The wavelength of the interface topography is 160 m, where its height is 60 m peak-to-peak. An explosive source is located 1100 m below the surface, as indicated by a black dot. The explosive source is modelled by adding a known value, whose time history is defined by the Gaussian source  $f(t) = \exp(-\alpha(t - t_0)^2)$ , with  $\alpha = 200$  and  $t_0 = 0.178$ , to the stresses ( $\sigma_x, \sigma_z$ ) at the centres of the four quadrangles around the point source. The sea bottom is at  $1300 \pm 30$  m depth. The models are made up of two grids of  $221 \times 181$  grid nodes each, with a grid spacing of 20 m in both the horizontal and the vertical directions; however, the grids of the second model are non-orthogonal for modelling the interface topography and the grid spacings near the interface are less than 20 m. The solid medium has a  $P$ -wave velocity of  $2000 \text{ m s}^{-1}$  and an  $S$ -wave velocity of  $1130 \text{ m s}^{-1}$ , and the liquid medium has a  $P$ -wave velocity of  $1500 \text{ m s}^{-1}$ . 15 grid points per minimum wavelength are used in the computations. Each computation takes 90 min on a 486 microcomputer when performing 800 time steps of 4 ms.

Seismograms of the vertical component of the particle velocity at the sea bottom for the two models are shown in Fig. 8. The seismogram in Fig. 8(a) shows a strong direct  $PS$  wave, a converted  $PS$  wave and a surface-reflected  $PP$  wave, as well as multiple reflected waves. Due to scattering at the rough sea bottom, the seismogram in Fig. 8(b) is not as clear as in Fig. 8(a). The direct wave and the surface-reflected wave can be identified.

Snapshots of the vertical component of the particle velocity at 800, 1280 and 1600 ms propagation time of the two models are shown in Figs 9 and 10. The snapshots of the model with a plane bottom (Fig. 9) show very clear wavefronts of the direct, reflected and transmitted as well as the converted  $PS$  waves. A decaying surface wave can be seen. Also, a Stoneley wave is found in the liquid area above the interface in the snapshots. In contrast, the snapshots of the model with a sinusoidal interface (Fig. 10) show, along with clear direct and transmitted and Stoneley wavefronts, a distorted converted  $PS$  wave and the interface-reflected wave. The converted  $PS$  wave and Stoneley wave are separated owing to the curved interface. Owing to its shorter wavelength the converted  $S$  wave is much more distorted than the transmitted  $P$  wave, as can be seen clearly in the snapshots.

### CONCLUSIONS

I have presented a quadrangle-grid velocity-stress finite-difference method for wave calculations with variable surface

topography. This work is based on the first-order velocity-stress hyperbolic system and a non-rectangular-grid finite-difference operator. The scheme uses non-orthogonal grids, thereby surface topography and curved interfaces can be incorporated easily. The method is stable for all values of Poisson's ratio. Liquid areas can be introduced inside the heterogeneous medium and the wave propagation in this mixed liquid-solid medium can be modelled using the same code as used for a solid. The comparison with analytic results shows that the numerical scheme is highly accurate. The numerical simulations show that the scheme is flexible in handling complex geometrical boundaries and the computational cost and storage requirements for the scheme are small. The numerical examples presented demonstrate clearly the wave phenomena which are caused by the corrugated surface or interface.

### ACKNOWLEDGMENTS

Thanks to the National Natural Science Foundation of China who supported this work. I also thank the anonymous reviewers for their helpful comments.

### REFERENCES

- Clayton, R. & Engquist, B., 1977. Absorbing boundary conditions for acoustic and elastic wave equations, *Bull. seism. Soc. Am.*, **67**, 1529–1540.
- Gottlieb, D., Gunzburger, M. & Turkel, E., 1982. On numerical boundary treatment of hyperbolic systems for finite difference and finite element methods, *SIAM J. Num. Anal.*, **19**, 671–682.
- Kelly, K.R., Ward, R.W., Treitel, S. & Alford, R.M., 1976. Synthetic seismograms: A finite-difference approach, *Geophysics*, **41**, 2–27.
- Kosloff, D., Kessler, D., Filho, A.Q., Tessmer, E., Behle, A. & Strahilevitz, R. 1990. Solution of the equations of dynamic elasticity by a Chebyshev spectral method, *Geophysics*, **55**, 734–748.
- Levander, A.R., 1988. Fourth-order finite-difference P–SV seismograms, *Geophysics*, **53**, 1425–1436.
- Magnier, S.-A., Mora, P. & Tarantola, A., 1994. Finite differences on minimal grids, *Geophysics*, **59**, 1435–1443.
- Moczo, P., 1989. Finite-difference technique for SH waves in 2-D media using irregular grids: application to the seismic response problem, *Geophys. J. Int.*, **99**, 321–329.
- Tessmer, E. & Kosloff, D., 1994. 3-D elastic modeling with surface topography by a Chebyshev spectral method, *Geophysics*, **59**, 464–473.
- Tessmer, E., Kosloff, D. & Behle, A., 1992. Elastic wave propagation simulation in the presence of surface topography, *Geophys. J. Int.*, **108**, 621–632.
- Virieux, J., 1986. P–SV wave propagation in heterogeneous media: Velocity-stress finite-difference method, *Geophysics*, **51**, 888–901.
- Zienkiewicz, O.C., 1977. *The Finite Element Method*, McGraw Hill, New York, NY.